Replicating Mg Scaffold via 3D Printing Sacrificial Template

Guanjin Li[a], Muhammad Hafizuddin Mustafa Marican[b], Soo Wah Gan[c], Tian Li[a], Lijie Zhang[a,d], Jiansheng Liu[d], Tao Li[b], Ching Chiuan Yen[c], Beng Wah Chua[b], Wei Zhai[a,]*

[a] *Department of Mechanical Engineering, National University of Singapore, 117575, Singapore*

[b] *Singapore Institute of Manufacturing Technology, Agency for Science, Technology and Research, 638075, Singapore*

[c] *NUS Centre for Additive Manufacturing, National University of Singapore, 117581, Singapore*

[d] *School of Advanced Manufacturing, Nanchang University, Nanchang 330031, China*

[*] *Corresponding author. Department of Mechanical Engineering, National University of Singapore, 117575, Singapore. Email address: mpezwei@nus.edu.sg (W. Zhai)*

Abstract

The fabrication of hierarchical and porous structures holds significant promise in biomedical science, aerospace, and related fields. Despite advancements in 3D printing technology that have enhanced the capability of complex porous structures, its application in metal fabrication remains challenging. In this paper, we introduce a method involving a 3D printed sacrificial template, created by the material extrusion process, for magnesium (Mg) infiltration. This method facilitates the production of porous Mg scaffolds, with the templates subsequently being water-leached. The morphology, shrinkage rate, compressive strength, and types of lattices of templates were observed and assessed to determine their viability. Further, comprehensive compression tests and cell adhesion experiments were conducted on the Mg scaffolds to evaluate their performance. The results suggest that the templates must possess adequate strength and continuous flow channels for successful Mg infiltration. The scaffolds experienced an average of about 30% shrinkage from the initial design to the final structure. The porous Mg scaffolds exhibit enhanced compressive strength (47.48±0.84 MPa) at lower porosity (0.52) and demonstrate satisfactory biocompatibility. This research highlights the efficacy and low cost of the template replication method in generating mechanically superior porous Mg scaffolds with customized pore sizes and structures. In future research, this method also holds promise for applications involving newly developed alloys.

Keywords: Template replication, 3D printing, Water-soluble salt, Biodegradable metal

1 Introduction

Nowadays, enhancing material performance while managing costs presents a significant challenge across diverse fields, spanning aerospace [1], biomedical science [2,3], and energy [4]. In response to this, researchers tried to devise strategies for optimizing material structures to achieve superior performance at reduced expenditures [3]. A notable strategy is the engineering of materials with porous or hierarchical architectures, which involves structuring materials at multiple scales to imbue them with distinct properties. However, traditional fabrication techniques, such as casting and forging, often face significant challenges in realizing the intricacy and specificity required by these advanced structures [5,6].

Three-dimensional printing (3D printing) [7,8], a cornerstone of additive manufacturing, is recognized for its capacity to fabricate complex geometries, minimize waste, and accelerate production processes. Some common 3D printing technologies include material extrusion (MEX) [9–11], vat photopolymerization (VPP) [12], powder bed fusion (PBF) [13–15], and so on. For instance, Hu Zhang [13] et al. reported a PBF method to fabricate Al–Cu–Mg alloy parts. However, the approach requires metal powders with an average diameter of 36 μm and must be conducted in an argon atmosphere, highlighting the elevated costs associated with metal part fabrication via 3D printing. Furthermore, this technology is limited by factors such as material variety, product size, surface finish, and final product performance. Addressing these limitations typically necessitates additional high cost manufacturing processes, including isostatic sintering and the use of additives.

Sacrificial template replication is an effective strategy with the advantages of low cost and shape complexity [16,17]. This method also facilitates material property enhancements during the liquid phase, leading to improved mechanical characteristics. Various sacrificial templates are utilized, including burn-out templates like carbon [18,19], polymeric sponges, and PU foams [20–22], as well as leachable templates like sodium chloride (NaCl) [23–26], sugar [27], calcium carbonate [28], and so on. Drawing inspiration from this method, sacrificial materials could be 3D printed to serve as a template used for molten metal infiltration, thereby indirectly creating intricately structured objects [23]. The incorporation of 3D printing technology further improves the complexity of templates. Currently, there are reports of employing 3D printed water-soluble inorganic salts as templates for fabricating materials like aluminium [29] or magnesium alloy [24].

The process of template replication method to fabricate porous materials is illustrated in Figure 1. This process commences with the 3D printing of a negative green body, followed by drying and sintering to yield the salt template. Subsequently, the materials are infiltrated into the template. After solidification, the template can be readily removed by dissolving the infiltrated portion in water, culminating in the production of porous materials.

This paper presents a method for the preparation of printable ink consisting of salt as the primary raw material, PVP as the binder, and ethanol as the solvent. This ink is specifically designed for the fabrication of sacrificial porous salt templates. Subsequently, magnesium alloy was infiltrated into the salt template. Upon solidification and template removal, magnesium porous scaffolds were successfully produced. The mechanical properties of the salt templates were comprehensively tested to assess their suitability for the infiltration process. This involved measuring the dimensions of the resulting magnesium scaffold and subjecting it to compression stress testing. Finally, the study conducted cell adhesion experiments to evaluate the biocompatibility of the fabricated materials.

2 Materials and Method

2.1 Materials

Salt particles were purchased from a local market. The polyvinyl pyrrolidone k-90 (PVP, Qingdao Usolf Chemical Technology Co., Ltd., China) was used as binder and Ethanol (Sigma-Aldrich, USA) was used as the solvent. NaOH was purchased from Sigma-Aldrich. The AZ31 magnesium and rabbit bone marrow stem cells (rBMSCs) were purchased from a local supplier.

2.2 Methods

2.2.1 Ink preparation

First, the salt particles were mixed with an aluminium oxide ball and subjected to initial breakage using a planetary ball mill machine (QM-WX04, CHISHUN, China). After ball milling, salt particles were sieved sequentially through 200-mesh screens. Subsequently, the obtained salt particles were collected and stored in a drying oven for future utilization.

The solvent was prepared by dissolving PVP in ethanol. Subsequently, the salt powder was introduced into the solvent to create the salt-based ink, which was then homogenized using a planetary mixer (SK-300SII, Kakuhunter, Japan). Detailed information regarding the mixing ratios of the materials can be found in Table S1.

2.2.2 3D printing of salt templates

The fabrication of the salt template (ST) was achieved using a commercial 3D printer (Allevi 3D, USA), with key parameters detailed in Table S2. A nozzle with an inner diameter of 410 μm was selected for extruding the salt-based ink. The printing path was meticulously designed and translated into a G-code file, which the printer could recognize and execute. Before commencing printing, the prepared salt-based ink was transferred into a syringe and compacted to eliminate any trapped air. During the printing process, the syringe's movement along the designated path was precisely controlled by mechanical systems. The salt-based ink was extruded under a controlled air pressure to form a 2D pattern, allowing for the layer-by-layer fabrication of lattice samples (Figure 1).

This study involved the design of five distinct types of STs, each with specified dimensions outlined in Table 1. Based on these dimensions, the designed relative density of the STs ($RD_{d\text{-}ST}$) and the designed relative density of the Mg scaffold ($RD_{d\text{-}M}$) were computed. Notably, the sum of $RD_{d\text{-}ST}$ and $RD_{d\text{-}M}$ equates to one.

Table 1 Design dimensions for five types of STs.

Type	a/μm	h/ μm	d/ μm	Designed RD of STs ($RD_{d\text{-}ST}$)	Designed RD of metal ($RD_{d\text{-}M}$)	Schematic of dimensions
ST-T1	700	600	410	0.628	0.372	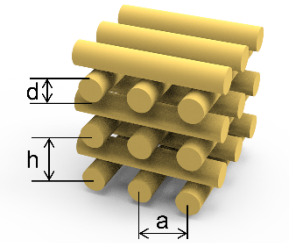
ST-T2	1000	600	410	0.440	0.560	
ST-T3	1500	600	410	0.293	0.707	
ST-T4	600/1000	600	410	0.550	0.450	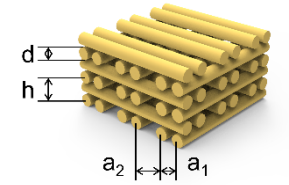
ST-T5	1000	600	410	0.440	0.560	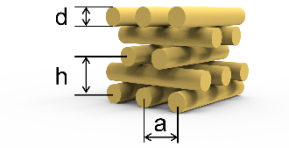

After printing, the green body STs were subjected to a four-hour drying period in a drying oven to eliminate any residual ethanol and facilitate the binding of salt particles by PVP. The dried STs were further sintered under 500, 600, and 750 ˚C to remove the binder to prevent decomposition in high-temperature environments and enhance the overall strength of the STs.

2.2.3 Infiltration of magnesium alloy

An aluminium alloy holder was employed to fix the samples' location in the square mould (Figure S1). Subsequently, the mould was preheated to 200 °C for 30 minutes. Before infiltration, the magnesium alloy (AZ31) ingot was fully melted and refined at 750 °C. Then, the molten Mg liquid was quickly poured into the mould, where it solidified under a pressure of 15 tons for 30 seconds. Next, the solidified metal block was rapidly cooled by immersion in water. After cutting down, the mixture of metallic Mg alloy and ST was obtained. Finally, the ST was dissolved by immersing the mixture in a 10 wt.% NaOH solution, mitigating the potential for severe corrosion reactions

involving Mg. The final Mg scaffolds were labelled as M-T1, M-T2. M-T3, M-T4, and M-T5 correspond to the different ST types used.

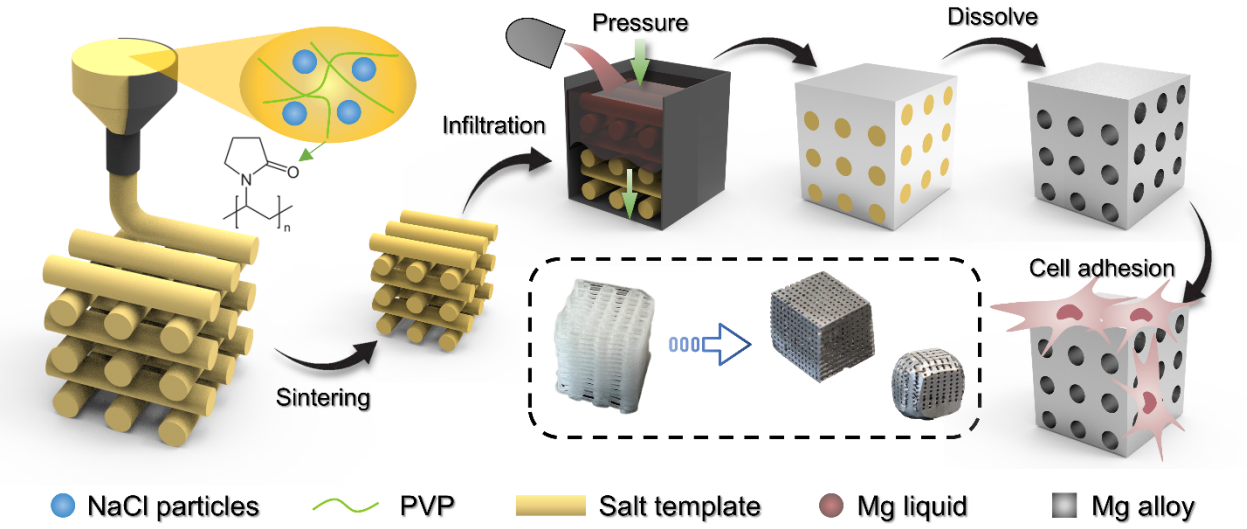

Figure 1 The process of 3D printed salt templating method.

2.2.4 Characterizations

The printability of salt-based slurry could be affected by the particle size and rheology. The salt particles were observed by a field emission scanning electron microscopy (FE-SEM, S-4300, Hitachi, Japan) and the rheology was measured by rheometer (HAAKE MARS rheometer, Thermo Scientific, USA). After printing, the structure of the sample was observed and measured by a digital microscope (VHX-6000, Keyence, Japan). The span distance was characterized by a 3D printed triangle support.

The sintering curve was determined by the thermogravimetry (TG) test. The structure of the green body and sintered sample was observed and measured by a digital microscope (VHX-6000, Keyence, Japan). The microstructure of samples was also observed by the FE-SEM. The shrinkage rate was further calculated according to the Eq. (1):

$$K = \frac{l_0 - l_1}{l_0} \times 100\% \quad (1)$$

Where the K is the shrinkage, l_0 and l_1 are original dimension (mm) and the dimension (mm) of sinter sample, respectively. Furthermore, the relative density of samples was calculated by Eq. (2):

$$\mathrm{RD} = \frac{V_s}{V_0} \tag{2}$$

Where the V_s and V_0 are the solid and overall volume of porous materials.

For characterizing the mechanical properties of samples, the compression test was carried out by a universal testing machine (Shimadzu AG25TB Testing Machine, Japan) with a loading rate of 50% strain/min. The engineering strain (ε) was calculated by Eq. (3) and the compressive stress (σ) was calculated by Eq. (4) as follows:

$$\varepsilon = \frac{h_f}{h_0} \times 100\% \tag{3}$$

$$\sigma = \frac{F}{l \times w} \tag{4}$$

Where h_0 is the initial height and h_f is the traveling distance of the indenter (mm). F is the loading force (N), l and w are the length and width (mm) of samples, respectively. The specific energy absorption (SEA, J/g) was calculated from Eq. (5) [30].

$$SEA = \frac{\int_0^{\varepsilon_d} \sigma \cdot d\varepsilon}{\rho_c \times RD} \tag{5}$$

Where ε_d is the densification strain, ρ_c is the density (g/cm^3) of the sample, and RD is the relative density of the sample.

The obtained Mg scaffolds were cut into plates measuring 10x10x2 mm and subsequently employed in a cell adhesion experiment. The plates were first sterilized through high-temperature water vapor treatment. Following sterilization, bone tissue stem cells were added to the samples, which were then placed in a constant temperature incubator. After a 24-hour incubation period, the samples were removed, allowed to dry, and subsequently observed using FE-SEM.

3 Result and disscusion

3.1 The rheology property of salt-based ink

Figure 2 shows the salt particles and the rheology test results. The particle shape, characterized by circularity, is crucial for ink flow dynamics [11,31–34]. Additionally, the particle size is

constrained by the nozzle diameter, since the ink must be extruded through this nozzle. After being broken and sieved, the processed salt particles, with an average size of approximately 20 μm, are depicted in Figure 2B.

Figure 2C also presents the inverse relationship between viscosity and shear rate. It can be observed that the viscosity of slurry decreases greatly with the increase of shear rate. The storage modulus (G') and loss modulus (G") are shown in Figure 2D, with the intersection of the G' and G" curves denoted by an "x". To the left of "x", the slurry exhibits solid-like behavior, whereas to the right, it behaves in a liquid-like manner [35]. This behavior signifies the slurry's capacity to be extruded in a liquid state and maintain form upon deposition (Figure 2A), a characteristic beneficial for the MEX process. With the high green body strength of the ink slurry, the ink can maintain the circular shape and the longest span distance on a triangle support is about 10 mm (Figure 2E). This attribute is essential for fabricating complex patterns with fine structural details. The role of PVP is to gel the ink and stabilize the particles within the ethanol matrix. During flow, the polymer chains disentangle under shear but revert to their entangled state when the stress is removed, leading to reduced viscosity at high shear rates. Upon drying, PVP acts to bind the particles together, thereby establishing the structural integrity of the green body [36].

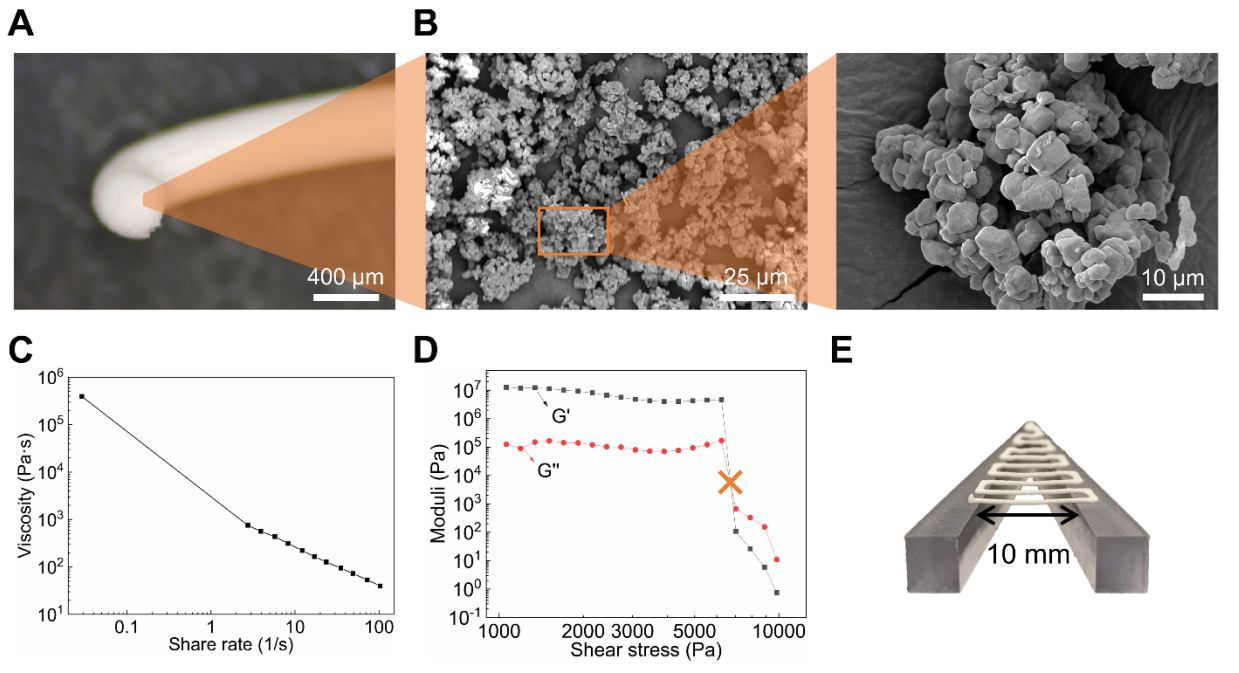

Figure 2 (A) The extruded salt ink, which maintained a circular shape. (B) The SEM images of salt particles, after being broken and sieved. (C) Log viscosity versus log shear rate of the salt-based ink. (D)

log storage modulus and log loss storage versus shear stress (the yield stress was marked as "x"). (E) The salt ink was extruded on a triangle support. The longest span distance was 10 mm.

3.2 Characterization of salt templates

Figure 3 presents the salt templates before and after sintering. Sintering serves a dual purpose: it not only forestalls the excessive generation of gases during the infiltration stage but also amplifies the mechanical robustness of the samples. After drying, the particles could be observed in a bonded state due to the presence of the PVP polymer (Figure 3A i and ii). Due to the volume reduction during drying, uneven surfaces could also be observed between the salt particles. The TG result (Figure S2) indicates a notable weight reduction of roughly 6.49% within the 300-500 °C temperature range. Referencing the weight content detailed in Table S1, this weight loss is attributable to the PVP polymer's thermal degradation within the aforementioned temperature window [37]. A further decline in mass is detected at 804 °C, marked by an endothermic transition in the heat flow curve, which is interpreted as the melting point of NaCl.

Taking into consideration the decomposition of PVP and to prevent the melting of samples, a preliminary sintering temperature range was established between 500 and 800 °C. Sintering at relatively low temperatures (500 and 600 °C) revealed the formation of noticeable holes on both the top surfaces (Figure 3B i and ii) and the cross-section (Figure 3D) of samples. This condition also led to the accentuation of particle edges and the emergence of some pores between the particles, indicative of an incomplete sintering process. The presence of these features is largely due to the burnout of the polymer during sintering, which results in insufficient particle densification [36]. When the sintering temperature was increased to 750 °C, the samples demonstrated a more compact surface morphology (Figure 3D and E) with significantly fewer pores when compared to those sintered at the lower temperatures. Additionally, the observed fractures were flat, with well-defined grain boundaries, suggesting a brittle fracture occurred along the crystalline structure, thereby implying that the particles formed strong inter-particular connections.

Additionally, the shrinkage rates at varying sintering temperatures (500, 600, and 750 °C) were quantitatively assessed, as depicted in Figure 3F. The data revealed that at sintering temperatures of 500 and 600 °C, the shrinkage rate was maintained below 5%. In contrast, a marked increase in the shrinkage rate to between 21.5% and 21.9% was observed when the samples were sintered at

750 °C. This enhanced shrinkage rate at the higher temperature is indicative of increased densification of the sample, suggesting that sintering at 750 °C results in a more densely packed structure as compared to sintering at the lower temperatures assessed.

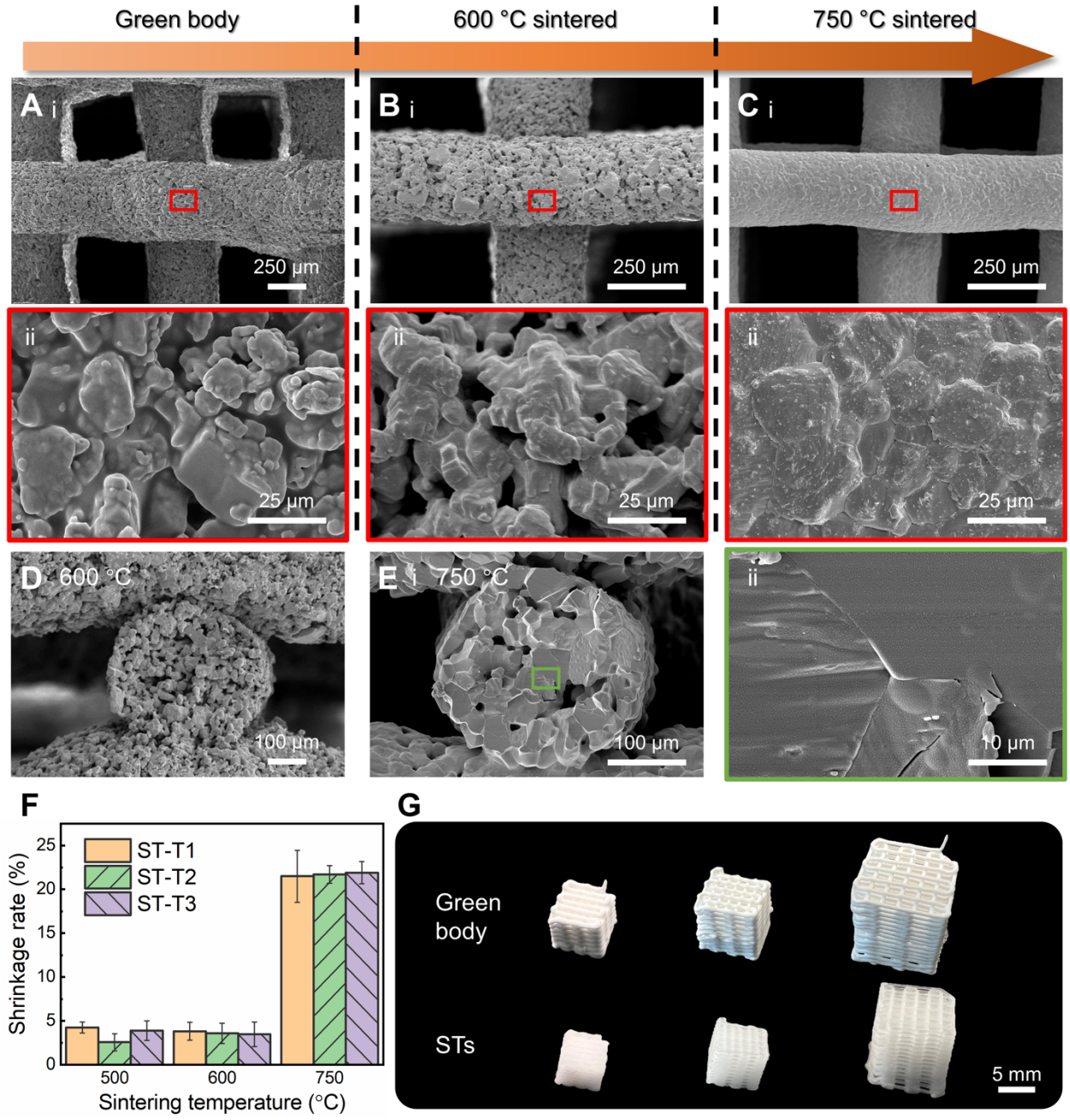

Figure 3 The top surfaces of (A) green body, (B) sintered sample under 600 °C, and (C) sintered sample under 750 °C. The side surfaces of sintered sample under (D) 600 °C and (E) 750 °C. (F) The result of sintering shrinkage with different sintering temperatures, and (G) the green body and sintered samples.

3.3 Infiltration of Mg scaffolds

Figure 4A shows the images of various lattice types of STs alongside their corresponding Mg scaffolds. This demonstrated that Mg liquid can faithfully replicate the structures of salt templates such as ST-T1 and ST-T2. However, the M-T3 shows a partially infiltrated monopoly. This is because of the low strength of ST-T3. As shown in Figure 4B, the compressive strength is the lowest (0.43±0.11 MPa), compared to the ST-T1 and ST-T2, which is 21.12±5.45 and 2.68±0.72 MPa, respectively. Furthermore, the stress-strain curves did not display yield plateaus after reaching the yield points, indicating that the samples exhibited a brittle fracture behavior. Additionally, the stress curve exhibited a tendency to decrease after fracture, which can be attributed to the layered lattice structure [30]. During the infiltration experiment involving ST-T3, the magnesium liquid initially entered the upper layer of the template but caused damage as it proceeded due to pressure exceeding the compressive strength of the template, resulting the partial infiltration.

Figure 4C shows the decreasing trend of relative density and the total shrinkage rate between the designed model and Mg scaffolds. Expected increases in relative density compared to the design porosity were observed due to dimension shrinkage during salt template sintering and magnesium alloy liquid solidification, as seen in Figure S3. The total shrinkage rates for T1 and T2 lattices from their designed dimensions to their final dimensions were 40.18±14.50% and 27.32±3.89%, respectively.

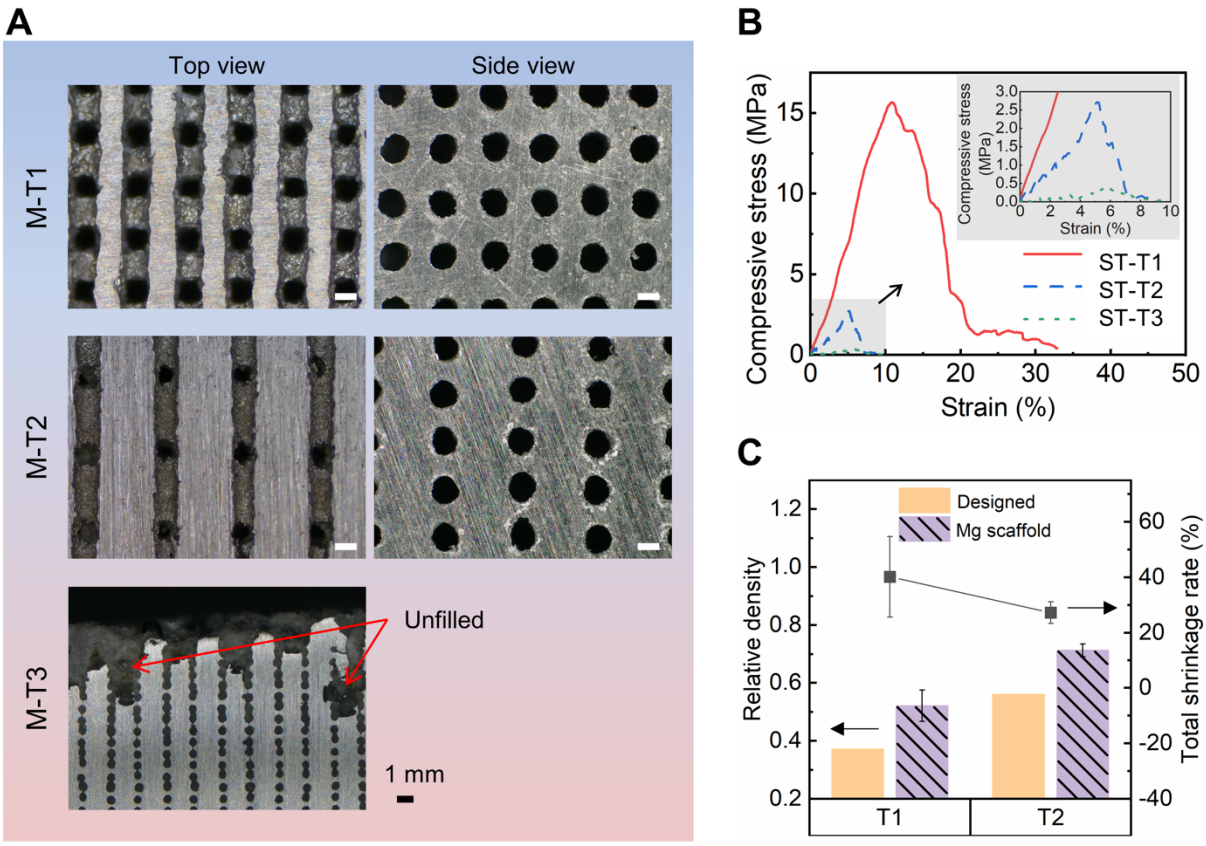

Figure 4 (A) The images of the Mg scaffold with different types of lattices. (B) The compression test of STs. (C) The relative density of the T1 and T2 lattice between the designed model and Mg scaffold, and the total shrinkage rate.

Figure 5 shows the infiltration process of the lattice with different patterns, offering insight into the relationship between the STs and Mg scaffolds. The metal was observed to fully penetrate the ST-T4 lattice, whereas ST-T5 undergoes structural failure during infiltration. It is because, in ST-T5, the lower struts impede the flow of the metallic liquid, inducing stress concentration that culminates in the collapse of the lattice, as shown in Figure 5B. The unsuitability of ST-T5 for infiltration is further evidenced by the interlocking struts, which obstruct the flow channels for the molten magnesium, causing the template to rapidly collapse when subjected to considerable pressure [38,39]. Therefore, it is critical for the template to have both sufficient structural integrity and appropriately designed flow channels to facilitate the infiltration of the molten magnesium solution.

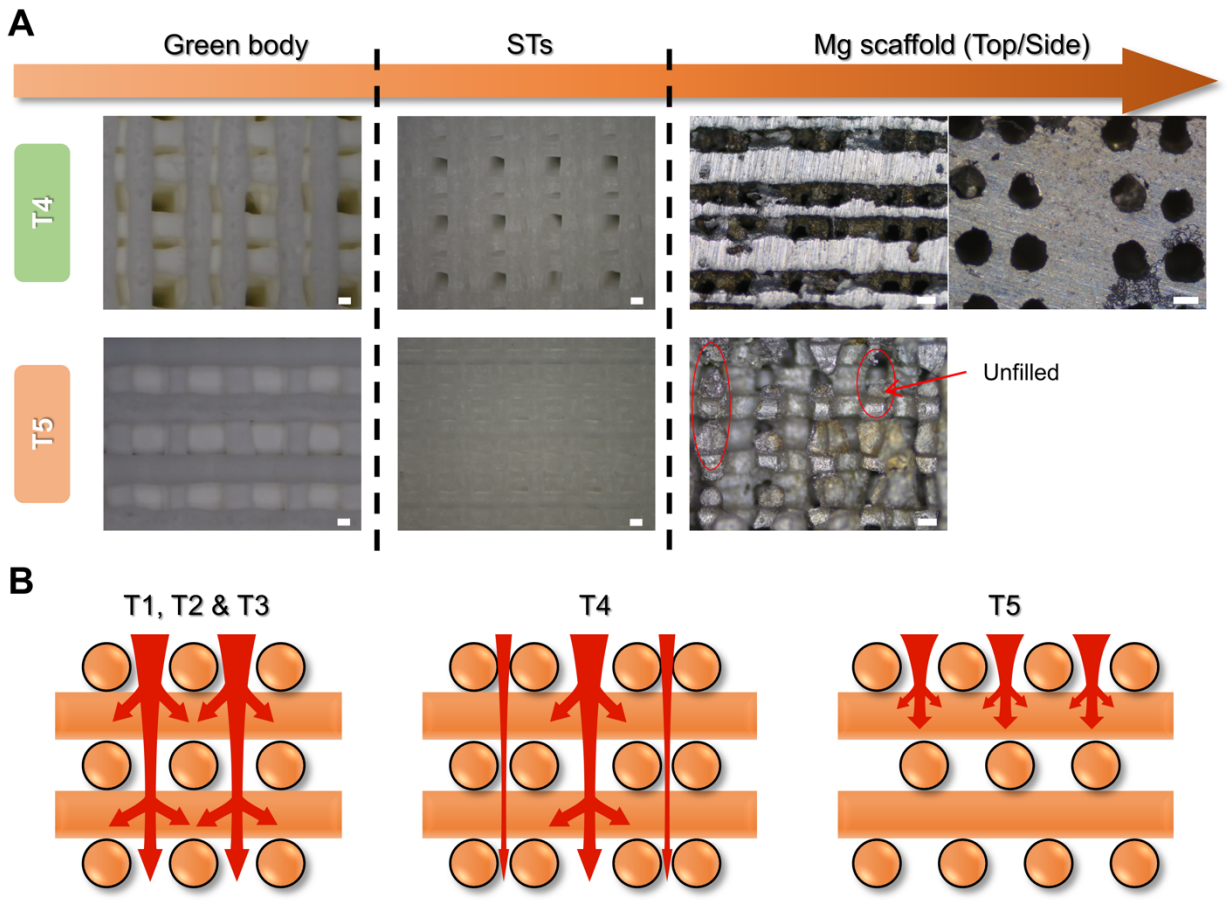

Figure 5 (A) The images of the T4 and T5 lattices and the corresponding green body, sintered sample, and Mg scaffold. The scale bars are 200 μm. (B) The infiltration process of different types of lattices.

3.4 Properties of Mg scaffold

Figure 6 shows the mechanical properties, surface morphology, and cell adhesion experiments of Mg scaffolds. The compressive test results, as shown in Figure 6a showed that the M-T1 scaffold (RD_{Mg} = 0.52±0.05) demonstrated a compressive strength of 47.48±0.84 MPa and a Young's modulus of 902.58±5.49 MPa. The SEA of the M-T1 before it was compacted reached 2323.47±194.07 $kJ \cdot m^{-3}$. Compared with other Mg scaffolds reported in other literature, the M-T1 still possessed a high strength with a low relative density, as evidenced in Figure 6B.

The inner morphology of M-T1 is shown in Figure 6C. Observations revealed a densely structured Mg scaffold with an inherently uneven morphology on the inner surface. This was due to the good wettability between the Mg liquid and salt template, allowing the liquid metal to replicate the texture of the salt template. This result signifies that the amalgamation of template replication with

die-casting techniques affords the production of samples with not only custom geometries but also enhanced structural strength.

Figure 6D shows the cell adhered to the M-T1 scaffold. The result indicated that bone stem cells remain viable and adhere to the scaffold's surface after 24 hours. The roughened surface of M-T1 also facilitated the cell attachment, which is favorable for tissue adhersion. Moreover, when placed in a simulated biological environment, the scaffold demonstrates a natural degradation behavior. Exploiting this degradation wisely, it is feasible to engineer bone implants that dissolve naturally in the body, thereby eliminating the necessity for post-healing surgical removal. Such materials have the potential to substantially alleviate patient discomfort and reduce the risks associated with treatment.

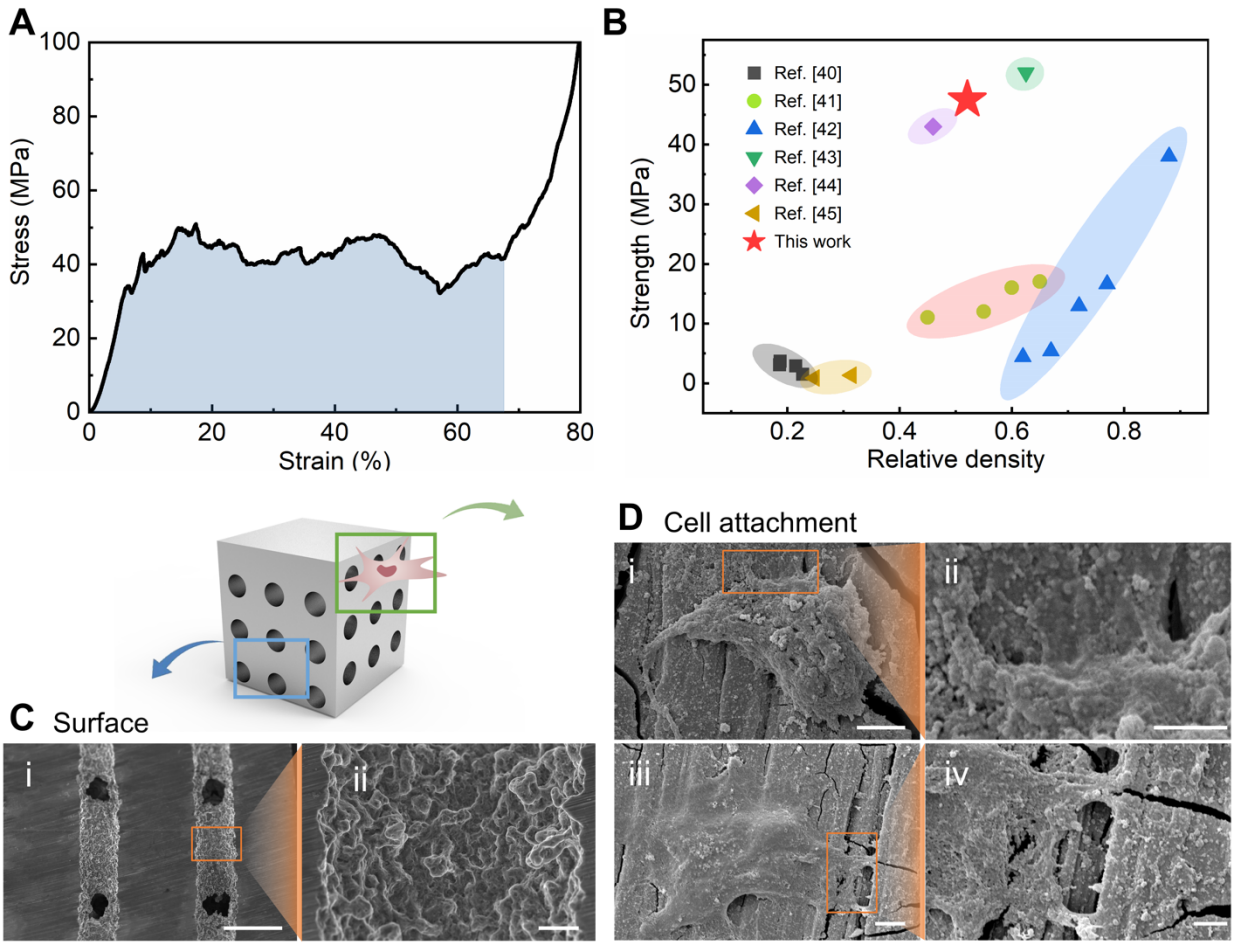

Figure 6 (A) The compression test of M-T1 scaffolds. (B) Compressive strength against the relative density of Mg scaffolds in this work with other reported materials [40–45]. The detailed data were listed in Table S3 (C) SEM image of i) the cross section and ii) the inner morphology of the Mg scaffold. The

scale bars are 500 μm and 50 μm, respectively. (D) The SEM image of Mg scaffolds after cell attachment experiments. i) and iii) are cells adhered to the Mg scaffold. The scale bars are 10 μm. ii) and iv) are the local details of the cells, respectively. The scale bars are 2 μm.

4 Conclusion

In this paper, a salt template was developed by a salt-based MEX process. The Mg scaffolds were obtained by immersing the melting Mg liquid into the salt template, followed by water leaching. The rheological properties of the ink, the shrinkage rate, and the compressive strength of the salt template were thoroughly investigated to determine the template's viability. Additionally, the dimensions of the infiltrated Mg scaffold were measured. The result indicates that the template infiltration method can be effectively utilized to fabricate Mg porous scaffolds with a specific porosity range and pore sizes. The structure of the Mg scaffold can be customized through 3D printing of the salt template. Furthermore, the cell adhesion test suggested that the Mg scaffold possessed good biocompatibility. Overall, this method allowed the preparation of porous magnesium alloys with small-sized pores and the appropriate tailoring of their structure. Critically, this method has the potential to be adapted for creating a diverse array of porous magnesium alloy supports, thereby laying the groundwork for the advancement of magnesium alloys with enhanced biological performances.

Acknowledgment

This research is supported by A*STAR under its IAF PP Grant (Project No. M22K4a0044) under the work package of “Thermal Management of Motor with Ferrofluid Composite Particles”.

References

[1] Rajamani MR, Punna E. Application of Weight, quality, cost, delivery, and productivity optimization techniques as an aerospace design for manufacturing and assembly guideline in the selection of alternate aerospace commercial off-the-shelf consumables. vol. 2020, 2020. https://doi.org/10.4271/2020-01-6002.

[2] Ingrole A, Aguirre TG, Fuller L, Donahue SW. Bioinspired energy absorbing material designs using additive manufacturing. Journal of the Mechanical Behavior of Biomedical Materials 2021;119:104518. https://doi.org/10.1016/j.jmbbm.2021.104518.

[3] Tetik H, Wang Y, Sun X, Cao D, Shah N, Zhu H, et al. Additive Manufacturing of 3D Aerogels and Porous Scaffolds: A Review. Advanced Functional Materials 2021;31:2103410. https://doi.org/10.1002/adfm.202103410.

[4] Li X, Li H, Fan X, Shi X, Liang J. 3D-Printed Stretchable Micro-Supercapacitor with Remarkable Areal Performance. Advanced Energy Materials 2020;10:1903794. https://doi.org/10.1002/aenm.201903794.
[5] Shi J, Akbarzadeh AH. Hierarchical cellular ferroelectric metamaterials: A design motif to enhance multifunctional figures of merit. Composite Structures 2020;250:112395. https://doi.org/10.1016/j.compstruct.2020.112395.
[6] Zhou M, Geng D. Multi-scale and multi-material topology optimization of channel-cooling cellular structures for thermomechanical behaviors. Computer Methods in Applied Mechanics and Engineering 2021;383:113896. https://doi.org/10.1016/j.cma.2021.113896.
[7] Rafiee M, Farahani RD, Therriault D. Multi-Material 3D and 4D Printing: A Survey. Advanced Science 2020;7.
[8] Siddique SH, Hazell PJ, Wang H, Escobedo JP, Ameri AAH. Lessons from nature: 3D printed bio-inspired porous structures for impact energy absorption – A review. Additive Manufacturing 2022;58:103051. https://doi.org/10.1016/j.addma.2022.103051.
[9] Mireles J, Kim H-C, Hwan Lee I, Espalin D, Medina F, MacDonald E, et al. Development of a fused deposition modeling system for low melting temperature metal alloys. Journal of Electronic Packaging, Transactions of the ASME 2012;134. https://doi.org/10.1115/1.4007160.
[10] Xu C, Chen X, Wu W, Liu Q, Ren L. Bioinspired Multi-Metal Structures Produced via Direct Ink Writing. Journal of Bionic Engineering 2022;19:1578–88. https://doi.org/10.1007/s42235-022-00257-2.
[11] Wang H, Chen C, Yang F, Shao Y, Guo Z. Direct ink writing of metal parts with curing by UV light irradiation. Materials Today Communications 2021;26. https://doi.org/10.1016/j.mtcomm.2021.102037.
[12] Mitteramskogler G, Schwentenwein M, Burkhardt C, Cruchley N. Lithography-based Metal Manufacturing (LMM) of 316L powder, 2020.
[13] Zhang H, Zhu H, Qi T, Hu Z, Zeng X. Selective laser melting of high strength Al–Cu–Mg alloys: Processing, microstructure and mechanical properties. Materials Science and Engineering: A 2016;656:47–54. https://doi.org/10.1016/j.msea.2015.12.101.
[14] Yin S, Fan N, Huang C, Xie Y, Zhang C, Lupoi R, et al. Towards high-strength cold spray additive manufactured metals: Methods, mechanisms, and properties. Journal of Materials Science and Technology 2024;170:47–64. https://doi.org/10.1016/j.jmst.2023.05.047.
[15] Das A, Ghosh A, Chattopadhyaya S, Ding C-F. A review on critical challenges in additive manufacturing via laser-induced forward transfer. Optics and Laser Technology 2024;168. https://doi.org/10.1016/j.optlastec.2023.109893.
[16] Murai K, Funamizu Y, Ogura T, Nishio K. Bioinspired mineralization of calcium carbonate in peptide hydrogel acting as a multifunctional three-dimensional template. Journal of Asian Ceramic Societies 2021;9:771–81. https://doi.org/10.1080/21870764.2021.1911060.
[17] Rebbecchi TA, Chen Y. Template-based fabrication of nanoporous metals. Journal of Materials Research 2018;33:2–15. https://doi.org/10.1557/jmr.2017.383.
[18] Kang Y, Baek D-H, Pyo S, Kim J. Carbon-Doped WO3 Nanostructure Based on CNT Sacrificial Template and its Application to Highly Sensitive NO2 Sensor. IEEE Sensors Journal 2020;20:5705–11. https://doi.org/10.1109/JSEN.2020.2973347.
[19] González-Sánchez M, Rivero-Antúnez P, Cano-Crespo R, Morales-Flórez V. Fabrication of Porous Alumina Structures by SPS and Carbon Sacrificial Template for Bone Regeneration. Materials 2022;15. https://doi.org/10.3390/ma15051754.

[20] Yang J-F, Zhang G-J, Kondo N, Ohji T, Kanzaki S. Synthesis of Porous Si3N4 Ceramics with Rod-Shaped Pore Structure. Journal of the American Ceramic Society 2005;88:1030–2. https://doi.org/10.1111/j.1551-2916.2005.00199.x.
[21] Wang H, Sung I, Li X, Kim D. Fabrication of Porous SiC Ceramics with Special Morphologies by Sacrificing Template Method. Journal of Porous Materials 2004;11:265–71. https://doi.org/10.1023/B:JOPO.0000046353.24308.86.
[22] Koç N, Timuçin M, Korkusuz F. Fabrication and characterization of porous tricalcium phosphate ceramics. Ceramics International 2004;30:205–11. https://doi.org/10.1016/S0272-8842(03)00090-7.
[23] Alison L, Menasce S, Bouville F, Tervoort E, Mattich I, Ofner A, et al. 3D printing of sacrificial templates into hierarchical porous materials. Sci Rep 2019;9:409. https://doi.org/10.1038/s41598-018-36789-z.
[24] Kleger N, Cihova M, Masania K, Studart AR, Löffler JF. 3D Printing of Salt as a Template for Magnesium with Structured Porosity. Advanced Materials 2019;31:1903783. https://doi.org/10.1002/adma.201903783.
[25] Kleger N, Fehlmann S, Lee SS, Dénéréaz C, Cihova M, Paunović N, et al. Light-Based Printing of Leachable Salt Molds for Facile Shaping of Complex Structures. Advanced Materials 2022;34:2203878. https://doi.org/10.1002/adma.202203878.
[26] Brothers AH, Dunand DC. Ductile Bulk Metallic Glass Foams. Advanced Materials 2005;17:484–6. https://doi.org/10.1002/adma.200400897.
[27] Ino K, Fukuda MT, Hiramoto K, Taira N, Nashimoto Y, Shiku H. Fabrication of three-dimensional calcium alginate hydrogels using sacrificial templates of sugar. Journal of Bioscience and Bioengineering 2020;130:539–44. https://doi.org/10.1016/j.jbiosc.2020.06.014.
[28] Li W, Ghazanfari A, McMillen D, Leu MC, Hilmas GE, Watts J. Fabricating ceramic components with water dissolvable support structures by the Ceramic On-Demand Extrusion process. CIRP Annals 2017;66:225–8. https://doi.org/10.1016/j.cirp.2017.04.129.
[29] Goodall R, Marmottant A, Salvo L, Mortensen A. Spherical pore replicated microcellular aluminium: Processing and influence on properties. Materials Science and Engineering: A 2007;465:124–35. https://doi.org/10.1016/j.msea.2007.02.002.
[30] Liu Q, Zhai W. Hierarchical Porous Ceramics with Distinctive Microstructures by Emulsion-Based Direct Ink Writing. ACS Appl Mater Interfaces 2022;14:32196–205. https://doi.org/10.1021/acsami.2c03245.
[31] Tang S, Yang L, Liu X, Li G, Jiang W, Fan Z. Direct ink writing additive manufacturing of porous alumina-based ceramic cores modified with nanosized MgO. Journal of the European Ceramic Society 2020;40:5758–66. https://doi.org/10.1016/j.jeurceramsoc.2020.07.058.
[32] Bowen JJ, Mooraj S, Goodman JA, Peng S, Street DP, Roman-Manso B, et al. Hierarchically porous ceramics via direct writing of preceramic polymer-triblock copolymer inks. Materials Today 2022. https://doi.org/10.1016/j.mattod.2022.07.002.
[33] Yang G, Sun Y, Limin qin, Li M, Ou K, Fang J, et al. Direct-ink-writing (DIW) 3D printing functional composite materials based on supra-molecular interaction. Composites Science and Technology 2021;215:109013. https://doi.org/10.1016/j.compscitech.2021.109013.
[34] Rao RB, Krafcik KL, Morales AM, Lewis JA. Microfabricated Deposition Nozzles for Direct-Write Assembly of Three-Dimensional Periodic Structures. Advanced Materials 2005;17:289–93. https://doi.org/10.1002/adma.200400514.

[35] Lewis JA. Colloidal Processing of Ceramics. Journal of the American Ceramic Society 2000;83:2341–59. https://doi.org/10.1111/j.1151-2916.2000.tb01560.x.
[36] Tang S, Yang Y, Fan Z, Yang L, Yang Z, Ling Q, et al. A novel composite binder design for direct ink writing alumina-based ceramics with enhanced strength at low sintering temperature. Ceramics International 2022;48:7963–74. https://doi.org/10.1016/j.ceramint.2021.11.343.
[37] Li G, Tang S, Yang L, Qian L, Liu F, Fan Z, et al. Fabrication of soluble salt-based support for suspended ceramic structure by layered extrusion forming method. Materials & Design 2019;183:108173. https://doi.org/10.1016/j.matdes.2019.108173.
[38] Facenda JC, Borba M, Corazza PH. A literature review on the new polymer-infiltrated ceramic-network material (PICN). Journal of Esthetic and Restorative Dentistry 2018;30:281–6. https://doi.org/10.1111/jerd.12370.
[39] Yang L-K, Jin Q, Guo R-F, Shen P. Exploiting bio-inspired high energy-absorbent metal/ceramic composites through emulsion-ice-templating and melt infiltration. Materialia 2020;14:100884. https://doi.org/10.1016/j.mtla.2020.100884.
[40] Lai Y, Li Y, Cao H, Long J, Wang X, Li L, et al. Osteogenic magnesium incorporated into PLGA/TCP porous scaffold by 3D printing for repairing challenging bone defect. Biomaterials 2019;197:207–19. https://doi.org/10.1016/j.biomaterials.2019.01.013.
[41] Wen CE, Yamada Y, Shimojima K, Chino Y, Hosokawa H, Mabuchi M. Compressibility of porous magnesium foam: dependency on porosity and pore size. Materials Letters 2004;58:357–60. https://doi.org/10.1016/S0167-577X(03)00500-7.
[42] Čapek J, Vojtěch D. Properties of porous magnesium prepared by powder metallurgy. Materials Science and Engineering: C 2013;33:564–9. https://doi.org/10.1016/j.msec.2012.10.002.
[43] Yazdimamaghani M, Razavi M, Vashaee D, Tayebi L. Development and degradation behavior of magnesium scaffolds coated with polycaprolactone for bone tissue engineering. Materials Letters 2014;132:106–10. https://doi.org/10.1016/j.matlet.2014.06.036.
[44] Cheng M, Wahafu T, Jiang G, Liu W, Qiao Y, Peng X, et al. A novel open-porous magnesium scaffold with controllable microstructures and properties for bone regeneration. Sci Rep 2016;6:24134. https://doi.org/10.1038/srep24134.
[45] Jia G, Hou Y, Chen C, Niu J, Zhang H, Huang H, et al. Precise fabrication of open porous Mg scaffolds using NaCl templates: Relationship between space holder particles, pore characteristics and mechanical behavior. Materials & Design 2018;140:106–13. https://doi.org/10.1016/j.matdes.2017.11.064.